

# *Explaining and predicting the Southern Hemisphere Eddy Driven Jet*

Article

Accepted Version

Mindlin, J., Shepherd, T. G. ORCID: <https://orcid.org/0000-0002-6631-9968>, Osman, M., Vera, C. S. and Kretschmer, M. ORCID: <https://orcid.org/0000-0002-2756-9526> (2025) Explaining and predicting the Southern Hemisphere Eddy Driven Jet. *Proceedings of the National Academy of Sciences of the United States of America*, 122 (29). e2500697122. ISSN 0027-8424 doi: 10.1073/pnas.2500697122 Available at <https://centaur.reading.ac.uk/123332/>

It is advisable to refer to the publisher's version if you intend to cite from the work. See [Guidance on citing](#).

To link to this article DOI: <http://dx.doi.org/10.1073/pnas.2500697122>

Publisher: National Academy of Sciences

All outputs in CentAUR are protected by Intellectual Property Rights law, including copyright law. Copyright and IPR is retained by the creators or other copyright holders. Terms and conditions for use of this material are defined in the [End User Agreement](#).

[www.reading.ac.uk/centaur](http://www.reading.ac.uk/centaur)

**CentAUR**

Central Archive at the University of Reading

Reading's research outputs online

# Explaining and predicting the Southern Hemisphere Eddy Driven Jet

Julia Mindlin<sup>a,1</sup>, Theodore G. Shepherd<sup>b,c</sup>, Marisol Osman<sup>d,e,f</sup>, Carolina S. Vera<sup>d,e,f</sup>, and Marlene Kretschmer<sup>a,b</sup>

This manuscript was compiled on June 17, 2025

The summertime Eddy Driven Jet (EDJ) in the Southern Hemisphere is a critical mediator between regional climate and large-scale phenomena, guiding synoptic systems that shape weather patterns. Uncertainties in global climate models (GCMs)—particularly in projecting changes in remote drivers like tropical warming, stratospheric polar vortex strengthening, and asymmetric tropical Pacific warming—hinder predictions of EDJ trends and associated regional outcomes. In this study, we develop a novel causal framework that combines observations, reanalysis datasets, and storylines estimated from the Coupled Model Intercomparison Project (CMIP) projections to attribute past EDJ changes and predict plausible future trajectories. Our findings indicate that tropical warming has evolved along the low end of plausible CMIP trajectories, while the stratospheric polar vortex shows robust strengthening, both strongly influencing observed EDJ trends. Our results suggest that 50% of the observed EDJ latitude shift can be directly attributed to global warming (GW), and the remaining 50% to remote drivers whose attribution to GW remains uncertain. Importantly, GCMs appear to accurately estimate the observed latitudinal shifts but underestimate the observed strengthening of the EDJ, while the proposed storylines are able to capture the observed trend. By integrating causal inference with climate storylines, our approach narrows the divide between attribution and prediction, offering a physically grounded method to estimate plausible pathways of future climate change.

The Southern Hemisphere's (SH) summertime Eddy Driven Jet (EDJ) is a critical feature of extratropical circulation that acts as a tropospheric mediator of the influence of remote drivers on regional climate (1, 2). The strength and latitudinal position of the SH EDJ in austral summer are among the circulation features with the most prominent forced response in both observations and models (3, 4). The zonal mean shift and strengthening observed in the last four decades has been attributed to ozone depletion (5–8). However, although ozone recovery is observable and zonal mean circulation trends have slowed down (9), the trends continue ((3, 10) and are presenting considerable zonal asymmetries (11, 12). This is in broad agreement with predictions from model simulations (10, 13–15) that anticipate a poleward shift and a strengthening of the EDJ as a robust response to CO<sub>2</sub> emissions (16–19). All phases of the Coupled Model Intercomparison Project (1, 10, 20, 21) project further strengthening and latitudinal shifts of the upper and lower SH westerlies for the remainder of the century.

Understanding the mechanisms that drive regional climate change is critical to improve projections and support decision-making in a rapidly warming world. General circulation

## Significance Statement

Accurate climate predictions are vital for preparing for future weather and regional climate changes, enabling communities and policymakers to make informed decisions to effectively address and adapt to climate change impacts. The Southern Hemisphere's summertime Eddy Driven Jet (EDJ) significantly influences weather patterns, but current climate models give conflicting messages concerning its future behavior due to uncertainties in remote drivers such as tropical warming and changes in the stratospheric polar vortex. Our study introduces a new method that combines real-world observations with climate model projections to better understand and predict changes in the EDJ. By identifying how different factors influence the EDJ, we explain and reduce the uncertainty in model predictions. This improved understanding provides more reliable near-term climate predictions, proposing a new way forward to evaluate model ensembles.

125	187
126	188
127	189
128	190
129	191
130	192
131	193
132	194
133	195
134	196
135	197
136	198
137	199
138	200
139	201
140	202
141	203
142	204
143	205
144	206
145	207
Author affiliations: <sup>a</sup> Leipzig Institute for Meteorology, Leipzig 04103, Germany; <sup>b</sup> Department of Meteorology, University of Reading, Reading RG6 6ET, United Kingdom; <sup>c</sup> Jülich Supercomputing Centre, Forschungszentrum Jülich, Jülich, Germany; <sup>d</sup> Departamento de Ciencias de la Atmósfera y los Océanos, Facultad de Ciencias Exactas y Naturales, Universidad de Buenos Aires, Buenos Aires C1428EGA, Argentina; <sup>e</sup> Centro de Investigaciones del Mar y la Atmósfera, Consejo Nacional de Investigaciones Científicas y Técnicas, Universidad Nacional de Buenos Aires, Buenos Aires C1428EGA, Argentina; <sup>f</sup> Instituto Franco Argentino sobre estudios de Clima y sus impactos (IFAEI-UMI3351), Centre National de la Recherche Scientifique, Buenos Aires C1428EGA, Argentina	208
150	209
151	210
152	211
153	212
154	213
155	214
156	215
157	216
158	217
159	218
JM conceptualization, analysis design, data curation and analysis, interpretation, original draft; TGS conceptualization, interpretation, editing; CSV interpretation; MO interpretation, editing; MK analysis design, interpretation, editing	219
160	220
161	221
162	222
163	223
The authors declare no competing interests.	224
164	225
To whom correspondence should be addressed. E-mail: julia.mindlin@uni-leipzig.de	226
165	227
166	228
167	229
168	230
169	231
170	232
171	233
172	234
173	235
174	236
175	237
176	238
177	239
178	240
179	241
180	242
181	243
182	244
183	245
184	246
185	247
186	248

models (GCMs) are indispensable tools for studying large-scale circulation responses to anthropogenic forcing. However, differences in the way that GCMs project large-scale circulation features can lead to significant variations in regional climate projections (22). The storyline approach provides a framework to infer plausible climatic changes with predictions that are conditional on the uncertain response of a few key drivers known to govern the targeted responses (23, 24). Large-scale remote drivers of the EDJ include tropical amplification of global warming, induced by tropical SST warming. This is associated with the expansion of the Hadley cell and the shift and strengthening of the extratropical storm tracks, both of which are linked to the EDJ (18, 25). This circulation change has in turn been associated with drying trends in the subtropical SH (1, 26). Another key driver is the stratospheric polar vortex, which modulates the position and trends of the SH EDJ and extratropical storm tracks (1, 27, 28), leading to increases in precipitation across mid-latitudes (1). Moreover, asymmetric warming trends of tropical Pacific sea surface temperatures (SST) drive atmospheric teleconnections that affect multiple regions and the EDJ in the Pacific basin (12, 29). Model disagreement in SST warming patterns can lead to large differences among the projected long-term precipitation trends across the globe (26, 30, 31). Finally, responses of these remote drivers also depend on the models' transient climate sensitivity and climate sensitivity to ozone depletion and recovery (21), providing an additional source of uncertainty.

Recognizing that uncertainties in the response of these drivers imply various plausible future climates can aid decision-makers (24, 32). The description of uncertainty in terms of a few storylines is a recent advance that calls for an attempt to constrain such storylines based on the observed trends. Constraining an ensemble of future storylines of the EDJ using observations would represent a 'conditional emergent constraint' on the EDJ response. However, constraints need to be anchored in physical understanding and causal relationships to be robust (33).

Here we use causal inference (34) to quantify the relationships between a set of well-documented large-scale drivers and the SH EDJ. We build upon previous work and only consider drivers for which storylines have already been proposed (1, 21, 30, 31). We focus on attributing EDJ trends over the period 1950–2023 and propose a novel approach to evaluate storylines by combining reanalysis datasets and observational products with the latest available CMIP projections. Finally, we assess whether specific ensembles of the proposed storylines can better explain the observed historical trends, as compared to the CMIP6 multi-model ensemble mean (MEM). Our approach provides the basis for a physically grounded dynamical attribution of recent EDJ changes, as well as constraints on dynamical storylines of plausible future changes. Given that model biases, for example in the jet latitude in the present climate, could influence the jet projected response (35), an assessment of plausible changes based on observed causal relationships and projected large-scale drivers offers a complementary approach to the intercomparison of model output.

## Results

**Causal analysis of remote driver influence on the EDJ.** The proposed causal network (CN) in Figure 1a represents our

causal hypotheses on the relationship between anthropogenic forcings, global warming, the proposed remote drivers, and the summer EDJ in the SH. Trends in the jet forced by anthropogenic greenhouse gases and ozone depleting substances are assumed to be mediated by forced trends in the stratospheric polar vortex (SPV), SST warming in the Central (CP) and Eastern tropical Pacific (EP), and tropical warming (TW). In addition, we consider a remaining direct effect of GW, which includes mediation from other unspecified mechanisms. We use detrended ERA5 data to estimate the causal effect between the remote drivers and the EDJ at each grid point, which yields a causal map for each link (Fig. 1b,  $RD \rightarrow u850, \beta_i(x)$  where  $x$  represents a grid cell). To test that these estimates are robust, we quantify the causal effects over different periods and in three reanalysis products (here we only show ERA5) as well as piControl simulations (see Methods) and report comparable results (see Figs. S1–S3 and Text S1 in Supporting Information). The only qualitative difference is found for  $GW \rightarrow u850$ . The GW index corresponds to the global average of surface temperature, which in the reanalysis captures a poleward shift of the westerly winds, while in piControl simulations the response is an equatorward shift (See Text S1 and Figs. S1–S5 in Supporting Information for further discussion). This is understandable because in piControl simulations the variations in GW are driven by internal variability rather than by external forcing, whereas in observations the linear detrending does not eliminate the forced response (Fig. S5). The residual effect of GW after linear detrending allows us to estimate the wind response to forced changes in GW. For the remainder of the article we will consider the causal link strengths estimated from linearly detrended ERA5 data (Fig. 1b) as our best estimate of the wind response to the drivers.

**Reconstruction and attribution of observed Eddy Driven Jet trends.** The estimated causal effects can be used to evaluate the time evolution of the EDJ as a linear combination of the  $u850$  response to the remote drivers' evolution  $\beta_i(x) \cdot RD_i(t)$ . We compute the latitude and strength of the EDJ in the zonal mean, the Pacific and the Atlantic-Indian basin for the period 1950–2023, resulting in six EDJ metrics. The trends and a large part of the internal variability are well captured by the reconstructions based on the causal drivers (black lines in left part of Figure 2). In particular, we capture the strong shift and weak strengthening in the Atlantic-Indian basin ( $-0.6$  deg/dec of latitude shift and  $0.3$  m/s/dec of strengthening in ERA5) as opposed to the smaller shift and stronger intensification over the Pacific basin ( $-0.33$  deg/dec and  $0.48$  m/s/dec in ERA5), previously described by (11). The relative contribution of each driver is shown in the bar plots in Figure 2. The individual driver contributions are estimated by evaluating the trends in jet metrics from reconstructions based on one driver at a time (Fig. 2 and Methods). In the zonal mean, we estimate that GW has directly contributed to one-half of the observed latitude shift, and the remaining shift is explained by TW and SPV strengthening, whose attribution to GW is left open for now. We further find that the latitude shift is large over the Atlantic basin (Fig. 2e), while the trend in the Pacific is smaller and mainly directly controlled by GW (Fig. 2c). The EP warming and SPV strengthening have a secondary effect (Fig. 2i) for this metric. The remote drivers TW and SPV, together with GW, explain the strengthening in the Pacific

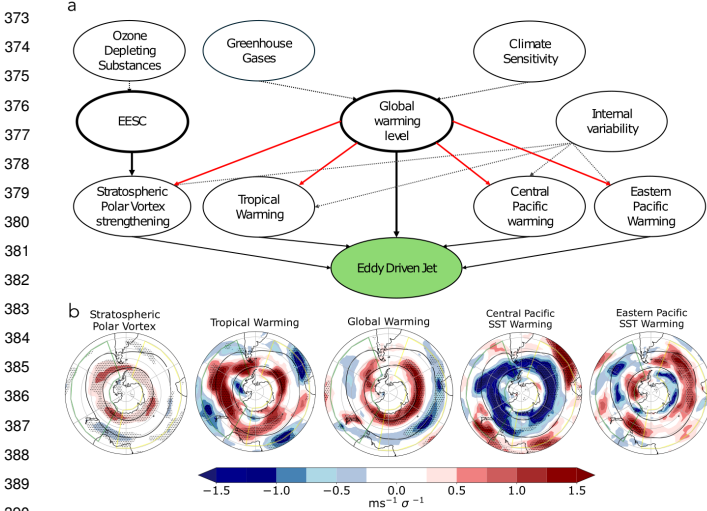


**Fig. 1.** (a) Assumed causal model for EDJ. The green sector indicates the part of the network that we quantify with reanalysis data and show in panel b. The gray sector indicates the part of the causal network where the links depend on the data generating process (i.e. in piControl there is no anthropogenic forcing) and for which we propose storylines. Dashed arrows indicate the influence of internal variability on the remote drivers, red arrows indicate that trends in the remote drivers can also be forced by global warming, solid arrows indicate causal effects from the remote drivers to the EDJ at each grid cell providing a causal map for each link ( $RD_i \rightarrow u850, \beta_i(x)$  where  $x$  represents a grid cell). (b) Causal maps for u850 estimated from detrended ERA5 reanalysis data. Stippling shows where the regression coefficients are significant above the 95% confidence level based on a Student's t-test.

basin while TW and EP warming control the strengthening in the Atlantic basin. Note that the role of ozone depletion is implicitly included in this attribution, as ozone depletion is the main driver of observed strengthening trends in the SPV (7).

To test whether the proposed CN can also reproduce modeled trends, we apply the same methodology and the same regression coefficients estimated from ERA5 (Fig. 1b) to reconstruct simulations of the period 1900-2099 using concatenated historical and scenario experiments from CMIP6 (Figures S6-S9). The reconstruction is based on the mean state and remote driver variability of the model, hence, the mean state bias in each model is preserved and the causal effect estimates are used to capture the variability around this mean state in response to changes in the drivers (see Methods, Text S2 and Figure S10 in SI). We find that there is a very high correlation between the reconstructed time series based on the drivers and the raw output of the models ( $r > 0.8$ , Fig. S8). Hence, the five included remote drivers are sufficient to explain, to a great extent, both the variability and the trends in both the observed and modeled SH circulation. Thus, it becomes imperative to attribute the observed remote driver trends.

**Constraining the uncertainty in GW level and SPV response to ozone depletion.** In the previous section, we attributed past EDJ changes to remote driver changes without distinguishing between internal variability and the forced component of remote driver trends. We now use CMIP6 simulations to evaluate what are the plausible forced responses in the remote drivers. Each combination of plausible remote driver responses will be referred to as a dynamical storyline (23). We then use

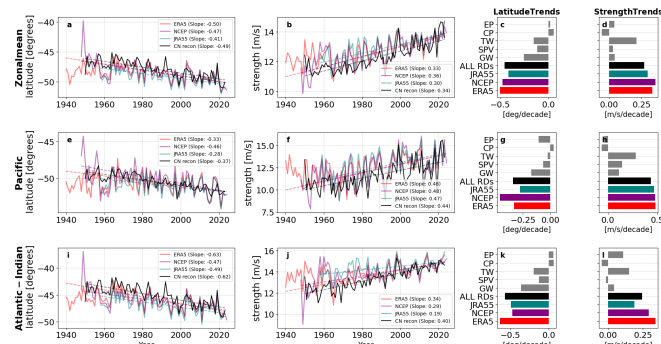


**Fig. 2.** Trends in EDJ metrics based on u850 (see Methods) estimated in three reanalysis products (colors) and reconstructed based on evolution of its causal drivers (black). (a) Latitude of the zonal-mean EDJ using data from ERA5 to estimate TW and SPV and ERSSTv5 to estimate CP and EP. (b) Same as (a) but for zonal-mean EDJ strength. (c,d) Contribution of remote drivers to the total trend in zonal mean latitude and strength metrics. (e-h) Same as (a-d) but for the Pacific basin only. (i-l) Same as (a-d) but for the Atlantic-Indian basin only. Latitude and strength trends are shown in deg/decade and m/s/decade respectively.

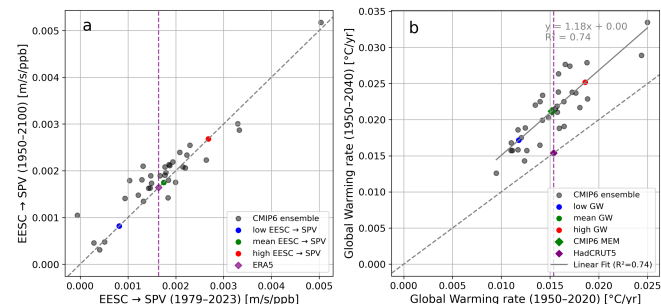


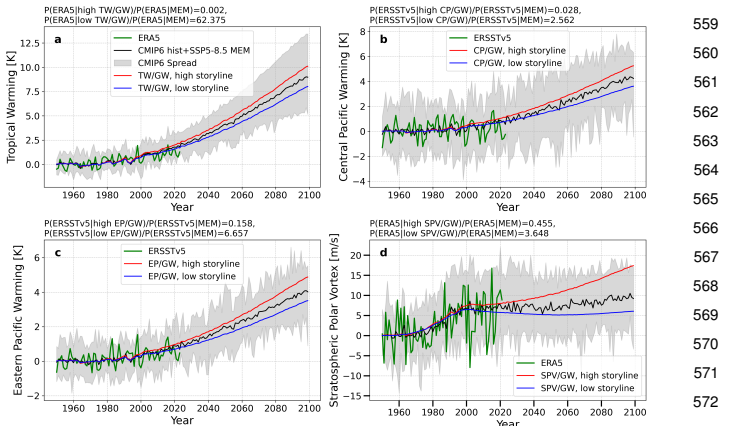
**Fig. 3.** (a) SPV sensitivity to equivalent effective stratospheric chlorine (EESC) for 1979-2023 vs. 1950-2100 in the CMIP6 ensemble, estimated via multiple linear regression with EESC and global warming (GW) as covariates. Color-coded are high (red), mean (green), and low (blue) SPV sensitivity, with ERA5 reanalysis in purple. (b) Rate of global mean surface temperature change for 1950-2020 vs. 1950-2040, with high (red), mean (green), and low (blue) GW storylines, and HadCRUT5 observed rates in purple.

497 observed trends in the remote drivers to discard some of the  
 498 storylines and thereby constrain the near-term projections. We  
 499 do this in two steps. In the first step we address uncertainty  
 500 in the GW level and SPV response to ozone depletion (bold  
 501 nodes in Fig. 1a).

502 Under the same emissions scenario, models exhibit differ-  
 503 ences in transient climate sensitivity, leading to differences in  
 504 GW rates and remote driver responses (Fig. 1a). Similarly,  
 505 under the same concentrations of ozone-depleting substances,  
 506 the SPV responds differently across models. However, we find  
 507 that in the models, the SPV sensitivity to EESC (EESC  $\rightarrow$   
 508 SPV) in the observed period (1979–2023) is almost perfectly  
 509 correlated with the SPV sensitivity in the full period (1950–  
 510 2100; Figure 3a), meaning that the observed sensitivity can  
 511 be used to constrain the future. As it happens, the observed  
 512 sensitivity is very close to the multi-model ensemble mean  
 513 (MEM) value. To isolate the role of remote driver uncertainty  
 514 in shaping EDJ changes from uncertainty in transient climate  
 515 sensitivity, we assess whether the GW rate in the recent past  
 516 exhibits predictive skill for near-term warming rates in the  
 517 model ensemble (Figure 3b). We find that the observed rate  
 518 of GW can be used to constrain the near-term future, and  
 519 that the observed GW rate (1950–2023) was very close to the  
 520 MEM value. Thus, we are justified in using the MEM value  
 521 for both GW and the (EESC  $\rightarrow$  SPV) sensitivity, as partial  
 522 emergent constraints.

523 To appreciate the effect of these constraints, we evaluate the  
 524 remote driver spread that can be captured if high/low GW and  
 525 high/low (EESC  $\rightarrow$  SPV) storylines are considered. Doing so  
 526 recovers the full range of remote driver responses in the CMIP6  
 527 ensemble (Fig. S11–12). Hence, by conditioning on (EESC  $\rightarrow$   
 528 SPV) and GW rate, we can eliminate the uncertainty arising  
 529 from model uncertainty in transient climate sensitivity and in  
 530 stratospheric response to ozone depletion.

531 **Constraining storylines of remote driver sensitivity to forcing**  
 532 **based on reanalysis and observations.** We showed that causal  
 533 effects of the remote drivers on the u850 winds can be estimated  
 534 from reanalysis and observations, and that the GW rate  
 535 and (EESC  $\rightarrow$  SPV) can be constrained by observations  
 536 and reanalysis (black solid arrows in Figure 1a). However,  
 537 the responses of the drivers to forcing (red arrows in Figure  
 538 1a) remain uncertain. As a second step to constrain this  
 539 uncertainty, we first estimate plausible storylines of remote  
 540 driver responses from the concatenated historical+SSP5-8.5  
 541 simulations from the CMIP6 ensemble (Fig. S13, Tab. S2,  
 542 Methods). Next, we treat each storyline as an hypothesis for  
 543 the observed forced trends and we evaluate if any of them can  
 544 explain the observed trends in remote drivers better than the  
 545 MEM. The modeled and observed time series of the remote  
 546 drivers are shown in Figure 4 together with the plausible  
 547 storylines estimated with the historical+SSP5-8.5 simulations  
 548 from the CMIP6 ensemble (Fig. S13, Tab. S2). We compare  
 549 the probabilities of observing each driver's trends under the  
 550 CMIP6 MEM and under a given extreme storyline. The ratio of  
 551 these probabilities, called Bayes Factor (see Methods) (36, 37),  
 552 indicates whether a given storyline derived from CMIP6 models  
 553 is more likely to explain the observed trends in the large-scale  
 554 driver than the MEM. By convention (36), a BF larger than  
 555 10 (or smaller than 0.1) indicates strong evidence (38–40)  
 556 in favor (or against) the hypothesis that a given storyline  
 557 matches the observed trend better than the MEM, whereas  
 558



559 **Fig. 4. Storylines of remote driver sensitivity to forcing.** (a) Tropical Warming (TW)  
 560 anomalies with respect to the 1950–1979 climatology in spliced (historical+SSP5-8.5)  
 561 CMIP6 simulations (gray shading), multi-model ensemble mean (MEM), high  
 562 and low TW storylines (red and blue respectively) and ERA5 data (green). (b) Same as  
 563 (a) but for the Stratospheric Polar Vortex (SPV). (c–e) Same as (b) but for Central  
 564 Pacific warming, Eastern Pacific warming estimated from the ERSSTv5 dataset. The  
 565 evolution of the remote driver (RD) under a high/low RD storyline is estimated as the  
 566 product of the storyline coefficient and  $\Delta T(t)$  where  $\Delta T(t)$  is the MEM global warming  
 567 time series estimated from the CMIP6 ensemble. The distribution for RDs is shown  
 568 in Figure S9 in Supporting Information and storyline coefficients are shown in Table  
 569 S2. The titles in each panel show Bayes Factor (BF) corresponding to each storyline,  
 570 that is, the ratio of the probability of observing the ERA5 or ERSSTv5 data given the  
 571 hypothesis that the climate is following a storyline vs. the probability of observing the  
 572 same given the hypothesis that the climate is following the MEM. For the estimation  
 573 of the Bayes Factors see Methods.

574 BFs in between can be interpreted as inconclusive. We find  
 575 that the observed TW is 62 times more likely to have occurred  
 576 if we followed the low TW storyline (blue line in Fig. 4a)  
 577 compared to the MEM response. The high/low SPV storylines  
 578 are as good as the MEM in explaining the observed response  
 579 (BFS between 0.1 and 10). The observed warming in the CP  
 580 and EP are slightly more likely to have occurred if we were  
 581 following the low CP and EP storylines, but this conclusion  
 582 depends on the observational product (Figs. S14 and S15 in  
 583 Supporting Information). Thus, while the reanalysis products  
 584 show evidence in favor of the low TW storylines, the SPV, CP  
 585 and EP storylines remain uncertain and the observed trends  
 586 do not provide enough evidence to constrain the ensemble.

587 **From explaining to predicting the Eddy Driven Jet.** In this last  
 588 section we use the constrained dynamical storylines to explain  
 589 and predict EDJ trends. We start by analyzing how models  
 590 simulate the EDJ in the recent past and near-term future (15  
 591 years ahead). Past EDJ trends are represented in the model  
 592 ensemble. However, we find that the ERA5 trends lie on the  
 593 edge of the full spread if all simulations are considered and  
 594 outside the distribution if model means are evaluated before  
 595 assessing latitude and strength trends (Fig. S16). This is  
 596 particularly true for the strengthening of the jet. Differences  
 597 in the models' responses can be recovered with the causal  
 598 network (Text S2 and Figures S5–9). However, the different  
 599 responses can arise not only from the remote driver spread,  
 600 but also from biases in the u850 mean state and variability  
 601 (Fig. S10), which makes it a challenge to take them at face  
 602 value.

603 To leverage our causal model of the EDJ (Fig. 1), we use  
 604 it to estimate the forced EDJ trends under each dynamical  
 605 ensemble member.

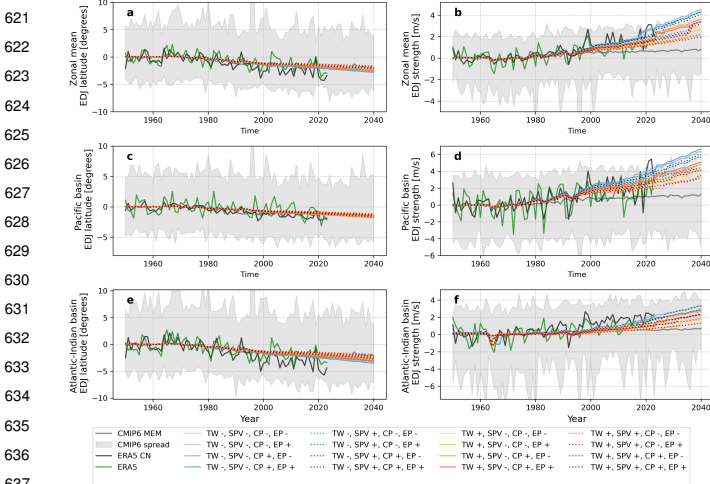


**Fig. 5.** (a) Total spread in the model mean EDJ latitude anomalies with respect to the 1950-1979 climatology are estimated from u850 in concatenated (historical+SSP5-8.5) CMIP6 simulations (gray shading), overlaid are the storylines projected until 2040 (color code) and anomalies with respect to the same period estimated from ERA5 reanalysis data (black). The storylines for which we find more evidence are shown with solid lines. (b) Same as (a) but for EDJ strength. (c,d) Same as (a,b) but for the Pacific basin. (e,f) Same as (a,b) but for the Atlantic-Indian basin.

storyline, assuming that the mean state and variability are fixed to those of ERA5 and the only source of uncertainty is the remote driver sensitivity to forcing. This acts as a third constraint on the storyline ensemble. Note that the EDJ responses evaluated for each storyline do not necessarily span the spread around the simulated CMIP6 mean. Instead, they span the uncertainty in the ERA5 EDJ that we can attribute to the uncertainty in the forced remote driver responses, which we estimated from CMIP6 and represented with an ensemble of dynamical storylines in the previous section. Figure 5 shows the zonal mean and basin jet metrics as described by the CMIP6 ensemble, the ERA5 reanalysis, the attributed component of ERA5 (as in Fig. 2) and an ensemble of EDJ storylines estimated as the linear combination of the storylines of remote driver trends and the causal pathways (see Methods). We estimate Bayes Factors again to compare the likelihood of observing the previously attributed ERA5 data under the hypothesis that we are following a given storyline as opposed to the hypothesis of being under the MEM (Figure 6).

We find that in particular the strengthening of the EDJ in all basins is better explained by any of the proposed storylines compared to the MEM, with larger BFs for almost all storylines ( $BF \geq 100$ ) and particularly higher BFs for the low TW. Only the latitude shift in the Pacific Basin is better explained by the MEM compared to all the storylines. In summary, all but one EDJ metric is better explained by the storylines than by the MEM (or the storylines are at least equally good). Moreover, the BFs of the latitude and strength metrics in the zonal mean and Atlantic basin confirm that low TW storylines better explain the observed trends.

Figure 7 shows the spatial pattern of observed wind changes per degree of warming and under the storylines with largest BFs (low TW and two opposite storylines of SPV, CP and EP warming). Spatially, these storylines present a strong latitude shift in the Atlantic-Indian basin and a strengthening in the Pacific basin, as reported by (11). The correlation

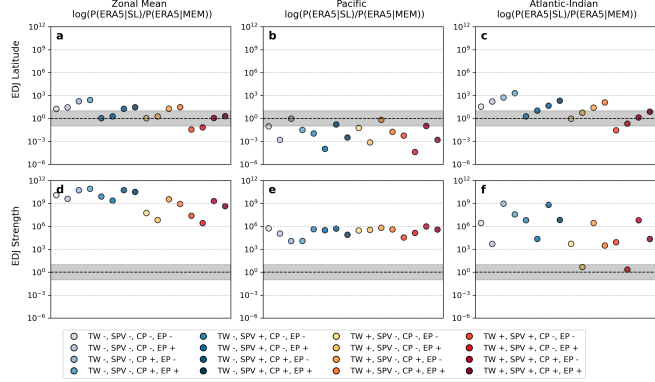


**Fig. 6.** (a-c) Logarithm of the Bayes Factor (BF) corresponding to each storyline, which quantifies to the ratio of the probability of observing the latitude change in ERA5 given the hypothesis that the climate is following a storyline vs. the probability of observing the ERA5 data given the hypothesis that the climate is following the MEM response. A  $\log(BF) \leq 1$  is interpreted as evidence in favor of the first hypothesis (in this case the storyline, white positive area) and  $\log(BF) \geq -1$  is interpreted as significant evidence in favor of the second hypothesis (in this case the MEM, negative white area) (36). The gray area is interpreted as no significant evidence in favor of either hypothesis. For the storyline calculation and the BF calculation, see Methods. The storylines are visualized in Figure 5. (d-f) Same as (a-c) but for the strength metric.

between the patterns is shown in Figure S20. Note that the NCEP reanalysis (Fig. 7b) presents a different spatial response compared to JRA55 (Fig. 7a) and ERA5 (Fig. 7c) and the response is more zonally symmetric. The strength of the MEM pattern of change per degree of warming (Fig. 7f) is much weaker than the storylines that we estimate (Fig. 7d,e). Moreover, the zonal asymmetries are not captured by the MEM, but they are captured by our proposed storylines. According to our dynamical storyline prediction, if we continue to follow the storylines for which we found more evidence in the previous section (low TW) the latitude and strength of the EDJ will remain above the values projected by the MEM while remaining inside the projected plume. We did not find sufficient evidence to constrain the uncertainty associated with SPV, CP and EP.

## Discussion

Our approach combining causal networks with storylines of the forced dynamical response has allowed us to explain and predict observed and simulated changes in the EDJ based on well-known relationships between key remote drivers and zonal winds at 850 hPa. It can be understood as complementary to what is known as the fingerprint method, which addresses the question “Has the climate change signal, associated with a particular forcing, emerged?” (41). Storylines represent distinct, physically plausible pathways through which large-scale atmospheric circulation may respond to anthropogenic forcing, acknowledging uncertainties in the precise nature of this response (19, 23). Instead of seeking the emergence of a single, predefined forced response - a key limitation of traditional fingerprinting methods due to model uncertainties - we expand the question to ask whether any plausible forced response has emerged and how it can be explained in terms of a small set of driver responses. The estimation of likelihood ratios, the Bayes Factors, is used to compare the agreement of observed remote driver responses with a set of potential

745 responses. This approach reframes the detection problem: 807  
 746 rather than validating a specific model response, we assess 808  
 747 whether observed changes align with one or more out of an 809  
 748 ensemble of several plausible forced responses. The BF can 810  
 749 be estimated for each year of data, adding each year a piece 811  
 750 of evidence (Fig. S21). We find that large differences between 812  
 751 the storylines that better explain observed trends deviate from 813  
 752 the CMIP6 MEM around the year 2000, suggesting a time of 814  
 753 emergence of the associated forced response. 815  
 754

755 The underlying hypothesis behind our causal network (Fig. 816  
 756 11a) is that the influence of the remote drivers on the EDJ 817  
 757 is the same when the variability of the drivers is generated 818  
 758 by internal variability or by anthropogenic forcing. This 819  
 759 is justified by other studies that address the sensitivity of 820  
 760 the EDJ to the same drivers in different time scales and 821  
 761 idealized simulations (12, 18, 28, 31, 42, 43). In addition, a 822  
 762 first approach to this question reveals that the causal pathway 823  
 763 strengths are stationary in the observed period (44) (Fig. 824  
 764 S4). In this respect, we consider the qualitative agreement 825  
 765 of the causal maps estimated from reanalysis and piControl 826  
 766 and the reproduction of the CMIP6 modeled trends in the 827  
 767 concatenated historical+SSP5-8.5 simulations (Fig. S7) as 828  
 768 sufficient evidence to work under this hypothesis. 829

769 The drivers demonstrate a better representation of EDJ 830  
 770 behavior in the South Pacific basin than in the Atlantic-Indian 831  
 771 basin, which highlights the need for future investigations 832  
 772 focusing into the role of the tropical Atlantic and Indian 833  
 773 oceans in driving observed jet strengthening in these regions. 834  
 774 Nevertheless, the causal framework allowed us to attribute 835  
 775 50% of the EDJ latitude shift directly to GW and 50% to the 836  
 776 remote drivers, and most of the strengthening to the remote 837  
 777 drivers (Fig. 2), with the role of GW in the remote driver 838  
 778 changes left open in this conditional attribution. Given that 839  
 779 EDJ uncertainty is associated not only with remote driver 840  
 780 responses to GW but also with transient climate sensitivity 841  
 781 and SPV response to ozone depletion, we showed that part 842  
 782 of the spread in EDJ responses can be constrained by the 843  
 783 observed rate of GW and of the sensitivity of the SPV to ozone 844  
 784 depleting substances (Fig. 3). The Bayes Factor estimates 845  
 785 suggest that the constrained storylines (regardless of the 846  
 786 particular remote driver responses) are more representative 847  
 787 of the emerging observed signal than is the CMIP6 MEM 848  
 788 (Figs. 4 and 5). Moreover, we find that the CMIP6 MEM 849  
 789 appears to underestimate the strengthening trends in the EDJ 850  
 790 (Figs. 6 and 7); the proposed storylines offer an alternative to 851  
 791 estimating projections of the EDJ. According to this analysis, 852  
 792 the observed strengthening EDJ trends do not necessarily 853  
 793 result from internal variability, but a predictable signal forced 854  
 794 by trends in large scale drivers, particularly in the Pacific 855  
 795 basin and the zonal mean. The approach is therefore aligned 856  
 796 with other recent work showing that predictable trends could 857  
 797 be larger than what models show if taken at face value (45). 858

798 In contrast to other dynamical storyline studies where 859  
 799 the storylines illustrate the spread in a model ensemble and 860  
 800 under a given warming level (23? ), our approach aims to 861  
 801 use the model simulations to understand the past and near- 862  
 802 term future, within the context of an observations-based 863  
 803 conditional attribution of the EDJ trends. Assumptions 864  
 804 behind the proposed storylines are that (1) EDJ trends are 865  
 805 controlled by the trends in the proposed drivers and their 866  
 806 influence is statistically stationary, (2) projections can be 867  
 807

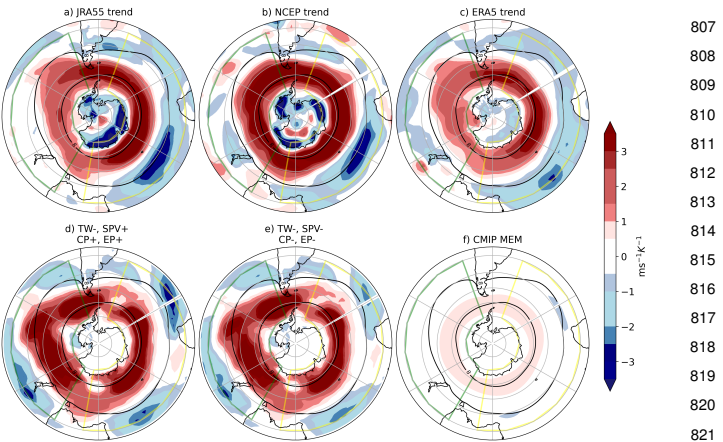


Fig. 7.  $u850$  response per degree of warming ( $ms^{-1} K^{-1}$ ). (a-c) are estimated from three reanalysis products as the change between the first and last 20 years of the total period for which we use ERA5 data to reconstruct storylines (1950-1973 vs. 2000-2023) multiplied by and divided by the level of warming in the same period, estimated in the same way. (d,e) Same as in (a-c) but for the plausible storylines of climate change related to low TW responses (11), (f) CMIP6 MEM response scaled per the degree of warming, evaluated in the same way as (a-c) for all each model individually and then averaged to get the ensemble mean.

constrained to the MEM GW rate and stratospheric response to ozone depletion/recovery. Future work could be directed to develop alternative approaches to near-term estimations that are not conditioned by these assumptions, such as storylines that systematically explore the possibility of remote driver responses changing over time. Given the potential impacts of underestimating the climate response to anthropogenic forcing at the regional scale (4), we find it imperative to use physical understanding to explore possible storylines that are not represented by the latest available CMIP simulations.

**Data and code.** Code is available via a [Github repository](#). All the data used for this study is publicly available.

**Materials.** We used the piControl (last 200 yrs of every simulation), the historical (1900-2014) and the SSP5-8.5 scenarios (2015-2099) from 33 CMIP6 models(46). We work with monthly outputs of zonal winds ( $ua$ ) at 850 hPa and 50 hPa, surface air temperature ( $tas$ ), upper tropospheric temperature ( $ta$ ) at 250 hPa and sea surface temperature ( $tos$ ). All model output are interpolated into a common grid of  $2.5^{\circ}$  using the ESMF area weighted scheme implemented in the Python Iris package. The downloading and preprocessing of the data was done using ESMValTool (47). For the estimation of the remote driver responses, we averaged all the available ensemble members available for each model (model mean) to reduce the influence of internal variability. When we refer to the multi-model ensemble mean we refer to the average of the model means. The list of models and ensemble members used can be found in Dataset S1.

To investigate the historical period we used the HadCRUT5 dataset(48) for global surface temperature, three different sea surface temperature (SST) observational datasets: the Hadley Centre Sea Ice and SST v.1.1 (HadISSTv1)(49), the Centennial In Situ Observation-Based Estimates of the Variability of SST and Marine Meteorological Variables v.2 (COBEv2)(49) and the National Oceanic and Atmospheric Administration Extended Reconstructed SST v.5 (ERSSTv.5)(50)

and three reanalysis: Japanese 55-year Reanalysis (JRA-55)(51), NCEP/NCAR reanalysis(52) and the extended ERA5 reanalysis(53). We mostly present results from ERA5, as this is the reanalysis which provides the longest time series, but the results are not sensitive to the choice of reanalysis and we show results for JRA55 and NCEP in the Supporting Information. The data from the reanalyses were interpolated into the common 2.5° grid for all the analyzes.

**Eddy Driven Jet metrics.** The latitude of the Eddy Driven Jet (EDJ) was calculated as the centroid of the zonal wind at 850 hPa between 30 and 70S(54). We quantified the latitude and strength of the zonally averaged EDJ and over the Pacific and Atlantic-Indian basins following (11), who showed that the observed trends in the Pacific basin have different trends than the zonal mean due to the influence of the tropical Pacific. The longitude bands we used were 210-80W for the Pacific basin and 40W-120E for the Atlantic-Indian basin.

$$\bar{\lambda} = \int_{70S}^{30S} \frac{\lambda [u(\lambda)]^2}{[u(\lambda)]^2} d\lambda \quad [1]$$

Wind strength is the wind strength at the EDJ latitude averaged over the different basins.

**Causal Inference.** We first proposed a causal model (Fig. 1a) of the EDJ based on the revision of published literature as interpreted by our expert judgment. In this causal model, internal variability and anthropogenic forcing are exogenous variables, and the remote drivers and the zonal winds (or metrics of the EDJ) in the SH are endogenous variables(55). To quantify causal pathways between the remote driver and the EDJ we fit a series of multiple linear regression (MLR) models where the covariates are the remote drivers and the target variable is either (1) the latitude or strength of the EDJ (which yields a scalar estimation for each metric, Table S1) or (2) the zonal wind at all grid cells in the Southern Hemisphere (which yields a set of causal maps, Table S1).

The MLR model for a (scalar) jet metric is:

$$EDJ'_{lat} = \sum_i \beta_i^{lat} RD'_i(t) + \epsilon_{lat}(t) \quad [2]$$

$$EDJ'_{str} = \sum_i \beta_i^{str} RD'_i(t) + \epsilon_{str}(t) \quad [3]$$

Wind strength is the wind strength at the EDJ latitude averaged over the different basins.

Where  $EDJ'_{metric}(t)$  is the metric standardized anomaly,  $RD'_i(t)$  are the standardized anomalies of the remote drivers and  $\epsilon_{metric}(t)$  are assumed Gaussian errors. The coefficients  $\beta_i^{metric}$  are estimated with an ordinary multivariate least squares algorithm implemented in the Python Stats package. To evaluate the spatial influence of the drivers on the zonal winds we use the same MLR model, but in this case fitted to each grid cell:

where  $u850'$  are the standardized anomalies of the seasonal average (December-February, DJF) of zonal winds and  $x$  represents grid cells and the apostrophe indicates that the

$$u850'(x, t) = \sum_i \beta_i(x) RD'_i(t) + \epsilon(x, t) \quad [4]$$

variable is standardized with respect to the mean and standard deviation of the whole period (1950-2023 for ERA5, 1950-2023 for JRA55 and 1958-2023 for NCEP). Estimated causal maps,  $\beta_i(x)$ , are standardized responses of zonal winds to one standard deviation in the time series of the remote driver and can be converted to physical units by multiplying them by the standard deviation of the winds at each grid cell.

In both the metric and spatial MLR, the  $RD'_i(t)$  are standardized anomalies of:

- Tropical Warming (TW), evaluated as the zonal average of temperature at 200 hPa between 15S and 15N in DJF,
- Stratospheric Polar Vortex (SPV) strength in October-November, evaluated as the zonal mean of the zonal wind strength at 50 hPa between 50S and 60S,
- The central Pacific (CP) and eastern Pacific (EP) sea surface temperature in DJF, evaluated as the sea surface temperature averaged over the boxes [5N-5S, 180-250E] and [0-10S, 260-280E] respectively in DJF and
- Global mean surface temperature (GW), the area weighted global average of surface air temperature in DJF.

Note that this approach does not exclude the possibility that causal links exist between the drivers, these are possible and certainly exist (suggested with thin red lines in Figure 1a), for example in the case of CP → TW (56). However, since the purpose of this article is not to describe the full network involving these drivers, we do not quantify these links. We rather use the estimated pathways to make estimates of  $u850'$  based on observed (Fig. 2) or proposed storylines (Fig. 4-6) for the remote drivers. The MLR framework ensures that by including all the drivers in the regression, the correct links are estimated(34, 55). We do not use the first 10 years of ERA5 data since it is reported that over the SH this early period is mainly statistical and a cold bias has been revealed in the stratosphere(57). The last value of the time series is December (2023) and January-February (2024).

**Constrain on the GW rate and SPV sensitivity to ozone depleting substances.** To evaluate the response of the stratospheric polar vortex (SPV) to external forcing, we perform a multiple linear regression of SPV anomalies onto global warming (GW) and equivalent effective stratospheric chlorine (EESC), following the approach of (21). The regression model is given by:

$$\Delta SPV(t) = a \Delta EESC(t) + b \Delta GW(t) + \epsilon, \quad [5]$$

where  $\Delta SPV(t)$  is the anomalous SPV index (e.g., zonal-mean zonal wind at 60°S, 10 hPa),  $\Delta EESC(t)$  is the polar EESC time series based on midlatitude mixing ratios from the WMO Scientific Assessment of Ozone Depletion (2014) (58), and  $\Delta GW(t)$  represents the global-mean surface temperature anomaly time series relative to 1950-1979. All time series

993 are anomalies are computed with respect to a 1950–1979  
 994 climatology.

995 The regression coefficients are computed separately for  
 996 each CMIP6 model over two periods: (1) the historical-to-  
 997 present interval (1979–2023) and (2) the full available time  
 998 span (1950–2100). The diagnosed sensitivity of SPV to  
 999 EESC forcing ( $a$  in Equation 5) is compared between the  
 1000 historical and future periods across the CMIP6 ensemble. This  
 1001 comparison is visualized via a scatter plot that contrasts SPV  
 1002 sensitivity to EESC in 1979–2023 versus 2080–2100 (Figure  
 1003 3a). The observed estimate from ERA5 is shown alongside  
 1004 the model distribution, and the relationship is benchmarked  
 1005 against a 1:1 line to assess potential shifts in SPV response  
 1006 under future conditions.

1007 To quantify the rate of global warming (GW) across the  
 1008 CMIP6 ensemble, we analyze model-specific time series of  
 1009 global surface temperature anomalies relative to the 1950–1979  
 1010 mean. For each model, temperature anomalies are fit with a  
 1011 second-order polynomial  $T(t) = at^2 + bt + c$  over two periods:  
 1012 1950–2020 and 1950–2040. The instantaneous rate of warming  
 1013 is then computed as the derivative of the fitted polynomial:

$$1015 \quad \frac{dT}{dt} = 2at + b, \quad [6]$$

1018 evaluated at the midpoint of each respective period (1985  
 1019 for 1950–2020, and 1995 for 1950–2040). This provides an  
 1020 estimate of the warming rate (in  $^{\circ}\text{C}/\text{year}$ ) under historical  
 1021 and near-future conditions. Observational warming rates are  
 1022 calculated using a quadratic fit to global DJF temperature  
 1023 anomalies from HadCRUT5, and the multi-model ensemble  
 1024 mean (MEM) rate is similarly computed from the average  
 1025 model temperature trajectory.

1026 **Storylines of remote driver responses.** The responses of the  
 1027 TW, CP and EP are estimated as the climatological change  
 1028 (1940–1969 vs. 2070–2099) in each of the drivers as defined in  
 1029 the last section scaled by the global mean surface temperature  
 1030 difference in the same period. The response of the SPV to  
 1031 forcing is estimated by regression of the SPV index onto GW  
 1032 and equivalent effective stratospheric chlorine as in 5.

1033 **Bayes Factors.** The probability of observing the trends of the  
 1034 last seven decades under each hypothesis (or storyline,  $H_1$ )  
 1035 can be contrasted to the probability of observing the data if  
 1036 the correct estimate for the remote driver responses were to  
 1037 be the MEM ( $H_0$ ) (39). The ratio of these two probabilities is  
 1038 the Bayes Factor:  $\text{BF} = \text{P}(\text{data}|H_1) / \text{P}(\text{data}|H_0)$ .

1039 Each of the hypothesis  $H_1$  is, by definition, a linear model  
 1040 of the driver sensitivity to GW:

$$1044 \quad \Delta RD_i^{sl}(t) = b_{sl} \Delta GW(t) + \epsilon \quad [7]$$

1047 where  $b_{sl}$  is the storyline coefficient ( $sl$  can be high or low,  
 1048 see Table S2) and  $\Delta GW(t)$  is the MEM  $\Delta GW(t)$  evolution.  
 1049 Except for SPV, for which the storylines are estimated as:

$$1052 \quad \Delta SPV_i^{sl}(t) = a \Delta EESC(t) + b_{sl} \Delta GW(t) \epsilon \quad [8]$$

1055 where  $a$  is the MEM SPV response to EESC ( $0.0018$   
 1056  $\text{ms}^{-1} \text{ppm}^{-1}$ ) and  $b_i$  is the storyline coefficient for the sto-  
 1057 rylines ( $H_1$ ). For the alternative hypothesis ( $H_0$ ) the RD time  
 1058 series is estimated as the MEM response. We assume that the  
 1059 year-to-year variability behaves as Gaussian noise, which we  
 1060 consider valid given that we checked that the detrended time  
 1061 series of these variables present no significant autocorrelation  
 1062 (Figure S22). If the noise is Gaussian, the probabilities  
 1063  $\text{P}(\text{data}|H_0)$  and  $\text{P}(\text{data}|H_1)$  can also be modeled with the  
 1064 Gaussian distribution:

$$1066 \quad P(\Delta RD_{obs}|H, b) = \frac{1}{\sqrt{2\pi}\sigma} \exp\left[\frac{(\Delta RD_{obs} - \Delta RD_{sl})}{2\sigma^2}\right] \quad [9]$$

$$1067 \quad = \frac{1}{\sqrt{2\pi}\sigma} \exp\left[-\left(\frac{SSE^2}{2\sigma^2}\right)\right] \quad [10]$$

1068 where  $\sigma^2$  is the variance of the year-to-year variability in the  
 1069 observed time series of each detrended remote driver anomaly  
 1070 (38, 40).

1071 **Reconstruction of  $u850$  storylines.** To estimate the evolution  
 1072 of  $u850_{sl}(x, t)$  under each storyline ( $sl$ ) we consider the mean  
 1073 state and variability to be that of ERA5 ( $\overline{u850_{ERA5}(x)}$  and  
 1074  $\sigma_{u850_{ERA5}(x)}$ ) and estimate the forced trends at each grid  
 1075 point using the causal maps  $\beta_i(x)$  estimated from ERA5 and  
 1076 the time series of each remote driver time series corresponding  
 1077 to each storyline  $RD_i^{sl}(t)$ :

$$1078 \quad u850'_{sl}(x, t) = \overline{u850_{ERA5}(x)} + \sum_i \beta_i(x) \sigma_{u850_{ERA5}(x)} RD_i^{sl}(t) \\ 1079 \quad + \epsilon(x, t) \quad [11]$$

1080 where  $sl$  represents the storyline coefficient (high/low). The  
 1081 time series of each remote driver is estimated as for the Bayes  
 1082 Factor calculation detailed above, where  $b_{sl}$  is the high/low  
 1083 value of the remote driver sensitivity to global warming (Figure  
 1084 S9 Supporting Information and Table S1). Given that we  
 1085 do not evaluate storylines of different GW rates, the MEM  
 1086  $\Delta GW(t)$  evolution is used to estimate the GW contribution.  
 1087 The Bayes Factor analysis in Figure 6 is performed in the  
 1088 same way as for the RDs, but with the EDJ metrics.

1089 **ACKNOWLEDGMENTS.** JM was funded by a PhD grant from  
 1090 CONICET during parts of this work, and would like to thank  
 1091 Pep Cos for his help with the use of ESMValTool. TGS and  
 1092 MK acknowledge funding from the European Commission Horizon  
 1093 2020 project XAIDA (Extreme Events: Artificial Intelligence for  
 1094 Detection and Attribution), Grant Agreement No. 101003469. MK  
 1095 further acknowledges funding from the Horizon Europe project  
 1096 EXPECT (Towards an Integrated Capability to Explain and Predict  
 1097 Regional Climate Changes), Grant Agreement No. 101137656.  
 1098 CSV and MO were funded by the Agencia Nacional de Promoción  
 1099 Científica y Tecnológica (grant no. PICT-2021-GRF-TI-00498),  
 1100 the Universidad de Buenos Aires (grant no. 20020220100075BA),  
 1101 and the Consejo Nacional de Investigaciones Científicas y Técnicas  
 1102 (CONICET) (grant no. PIP11220200102038CO).

1103 1. J. Mindlin, et al., Storyline description of Southern Hemisphere midlatitude circulation and  
 1104 precipitation response to greenhouse gas forcing. *Clim. Dyn.* **54**, 4399–4421 (2020).

1105 2. H. Nguyen, et al., Variability of the extent of the Hadley circulation in the southern hemisphere:  
 1106 a regional perspective. *Clim. Dyn.* **50**, 129–142 (2018).

1117 3. T Woollings, M Drouard, CH O'Reilly, DMH Sexton, C McSweeney, Trends in the atmospheric  
1118 jet streams are emerging in observations and could be linked to tropical warming. *Commun.  
1119 Earth & Environ.* **4**, 125 (2023).

1120 4. TA Shaw, et al., Emerging Climate Change Signals in Atmospheric Circulation. *AGU Adv.* **5**,  
1121 e2024AV001297 (2024).

1122 5. DWJ Thompson, S Solomon, Interpretation of Recent Southern Hemisphere Climate Change.  
1123 *Science* **296**, 895–899 (2002).

1124 6. JM Arblaster, GA Meehl, Contributions of External Forcings to Southern Annular Mode  
1125 Trends. *J. Clim.* **19**, 2896–2905 (2006).

1126 7. S Son, et al., Impact of stratospheric ozone on Southern Hemisphere circulation change: A  
1127 multimodel assessment. *J. Geophys. Res. Atmospheres* **115**, 2010JD014271 (2010).

1128 8. S Lee, SB Feldstein, Detecting Ozone- and Greenhouse Gas-Driven Wind Trends with  
1129 Observational Data. *Science* **339**, 563–567 (2013).

1130 9. A Banerjee, JC Fyfe, LM Polvani, D Waugh, KL Chang, A pause in Southern Hemisphere  
1131 circulation trends due to the Montreal Protocol. *Nature* **579**, 544–548 (2020).

1132 10. A Ossó, et al., Advancing Our Understanding of Eddy-driven Jet Stream Responses to  
1133 Climate Change – A Roadmap. *Curr. Clim. Chang. Reports* **11**, 2 (2024).

1134 11. DW Waugh, A Banerjee, JC Fyfe, LM Polvani, Contrasting Recent Trends in Southern  
1135 Hemisphere Westerlies Across Different Ocean Basins. *Geophys. Res. Lett.* **47**,  
e2020GL088890 (2020).

1136 12. D Yang, JM Arblaster, GA Meehl, MH England, The Role of Coupled Feedbacks in the  
1137 Decadal Variability of the Southern Hemisphere Eddy-Driven Jet. *J. Geophys. Res.  
1138 Atmospheres* **126**, e2021JD035023 (2021).

1139 13. PJ Kushner, IM Held, TL Delworth, Southern Hemisphere Atmospheric Circulation Response  
1140 to Global Warming. *J. Clim.* **14**, 2238–2249 (2001).

1141 14. JH Yin, A consistent poleward shift of the storm tracks in simulations of 21st century climate.  
1142 *Geophys. Res. Lett.* **32**, 2005GL023684 (2005).

1143 15. GK Vallis, P Zurita-Gotor, C Cairns, J Kidston, Response of the large-scale structure of the  
1144 atmosphere to global warming. *Q. J. Royal Meteorol. Soc.* **141**, 1479–1501 (2015).

1145 16. G Chen, IM Held, Phase speed spectra and the recent poleward shift of Southern  
1146 Hemisphere surface westerlies. *Geophys. Res. Lett.* **34**, 2007GL031200 (2007).

1147 17. EP Lim, I Simmonds, Effect of tropospheric temperature change on the zonal mean  
1148 circulation and SH winter extratropical cyclones. *Clim. Dyn.* **33**, 19–32 (2009).

1149 18. AH Butler, DWJ Thompson, R Heikes, The Steady-State Atmospheric Circulation Response  
1150 to Climate Change-like Thermal Forcings in a Simple General Circulation Model. *J. Clim.* **23**,  
3474–3496 (2010).

1151 19. TA Shaw, Mechanisms of Future Predicted Changes in the Zonal Mean Mid-Latitude  
1152 Circulation. *Curr. Clim. Chang. Reports* **5**, 345–357 (2019).

1153 20. TJ Bracegirdle, et al., Twenty first century changes in Antarctic and Southern Ocean surface  
1154 climate in CMIP6. *Atmospheric Sci. Lett.* **21**, e984 (2020).

1155 21. J Mindlin, TG Shepherd, C Vera, M Osman, Combined Effects of Global Warming and Ozone  
1156 Depletion/Recovery on Southern Hemisphere Atmospheric Circulation and Regional  
1157 Precipitation. *Geophys. Res. Lett.* **48**, e2021GL092568 (2021).

1158 22. TG Shepherd, Atmospheric circulation as a source of uncertainty in climate change  
1159 projections. *Nat. Geosci.* **7**, 703–708 (2014).

1160 23. G Zappa, TG Shepherd, Storylines of Atmospheric Circulation Change for European  
1161 Regional Climate Impact Assessment. *J. Clim.* **30**, 6561–6577 (2017).

1162 24. TG Shepherd, Storyline approach to the construction of regional climate change information.  
1163 *Proc. Royal Soc. A: Math. Phys. Eng. Sci.* **475**, 20190013 (2019).

1164 25. BJ Harvey, P Cook, LC Shaffrey, R Schiemann, The Response of the Northern Hemisphere  
1165 Storm Tracks and Jet Streams to Climate Change in the CMIP3, CMIP5, and CMIP6 Climate  
1166 Models. *J. Geophys. Res. Atmospheres* **125**, e2020JD032701 (2020).

1167 26. C Junquas, CS Vera, L Li, H Le Treut, Impact of projected SST changes on summer rainfall in  
1168 southeastern South America. *Clim. Dyn.* **40**, 1569–1589 (2013).

1169 27. NJ Byrne, TG Shepherd, Seasonal Persistence of Circulation Anomalies in the Southern  
1170 Hemisphere Stratosphere and Its Implications for the Troposphere. *J. Clim.* **31**, 3467–3483  
1171 (2018).

1172 28. P Cepi, TG Shepherd, The Role of the Stratospheric Polar Vortex for the Austral Jet  
1173 Response to Greenhouse Gas Forcing. *Geophys. Res. Lett.* **46**, 6972–6979 (2019).

1174 29. D Yang, et al., Role of Tropical Variability in Driving Decadal Shifts in the Southern  
1175 Hemisphere Summertime Eddy-Driven Jet. *J. Clim.* **33**, 5445–5463 (2020).

1176 30. R Ghosh, TG Shepherd, Storylines of Maritime Continent dry period precipitation changes  
1177 under global warming. *Environ. Res. Lett.* **18**, 034017 (2023).

1178 31. J Mindlin, CS Vera, TG Shepherd, M Osman, Plausible Drying and Wetting Scenarios for  
1179 Summer in Southeastern South America. *J. Clim.* **36**, 7973–7991 (2023).

1180 32. E Baulenas, G Versteeg, M Terrado, J Mindlin, D Bojovic, Assembling the climate story: use  
1181 of storyline approaches in climate-related science. *Glob. Challenges* **7**, 2200183 (2023).

1182 33. A Hall, P Cox, C Huntingford, S Klein, Progressing emergent constraints on future climate  
1183 change. *Nat. Clim. Chang.* **9**, 269–278 (2019).

1184 34. M Kretschmer, et al., Quantifying Causal Pathways of Teleconnections. *Bull. Am. Meteorol.  
1185 Soc.* **102**, E2247–E2263 (2021).

1186 35. EA Barnes, DL Hartmann, DMW Frierson, J Kidston, Effect of latitude on the persistence of  
1187 eddy-driven jets. *Geophys. Res. Lett.* **37**, 2010GL043199 (2010).

1188 36. AM Ellison, An Introduction to Bayesian Inference for Ecological Research and Environmental  
1189 Decision-Making. *Ecol. Appl.* **6**, 1036–1046 (1996).

1190 37. S Shikano, Hypothesis Testing in the Bayesian Framework. *Swiss Polit. Sci. Rev.* **25**,  
288–299 (2019).

1191 38. M Kretschmer, G Zappa, TG Shepherd, The role of Barents–Kara sea ice loss in projected  
1192 polar vortex changes. *Weather. Clim. Dyn.* **1**, 715–730 (2020).

1193 39. TG Shepherd, Bringing physical reasoning into statistical practice in climate-change science.  
1194 *Clim. Chang.* **169**, 2 (2021).

1195 40. X Shen, M Kretschmer, TG Shepherd, A Forensic Investigation of Climate Model Biases in  
1196 Teleconnections: The Case of the Relationship Between ENSO and the Northern  
1197 Stratospheric Polar Vortex. *J. Geophys. Res. Atmospheres* **129**, e2024JD041252 (2024).